Available online at www.sciencedirect.com

jmr&t Journal of Materials Research and Technology

journal homepage: www.elsevier.com/locate/jmrt

Application of machine learning to object manipulation with bio-inspired microstructures

Manar Samri [a,b], *Jonathan Thiemecke* [a], *René Hensel* [a], *Eduard Arzt* [a,b,c,*]

[a] *INM – Leibniz Institute for New Materials, Campus D2 2, 66123 Saarbrücken, Germany*

[b] *Department of Materials Science and Engineering, Saarland University, Campus D2 2, 66123 Saarbrücken, Germany*

[c] *Department of Mechanical and Aerospace Engineering, Program in Materials Science and Engineering, University of California, San Diego, CA 92093, USA*

ARTICLE INFO

Article history:
Received 24 March 2023
Accepted 30 September 2023
Available online 6 October 2023

Keywords:
Bioinspired-adhesives
Microstructures
Pick and place
Machine learning
Classification

ABSTRACT

Bioinspired fibrillar adhesives have been proposed for novel gripping systems with enhanced scalability and resource efficiency. Here, we propose an in-situ optical monitoring system of the contact signatures, coupled with image processing and machine learning. Visual features were extracted from the contact signature images recorded at maximum compressive preload and after lifting a glass object. The algorithm was trained to cope with several degrees of misalignment and with unbalanced weight distributions by off-center gripping. The system allowed an assessment of the picking process for objects of various mass (200, 300, and 400 g). Several classifiers showed a high accuracy of about 90 % for successful prediction of attachment, depending on the mass of the object. The results promise improved reliability of handling objects, even in difficult situations.

1. Introduction

We are right on the edge of the fourth industrial revolution. As industries are transitioning towards automation and digitalization of their production lines, the need for smart grippers has grown rapidly. The goal for this transformation is to increase efficiency, speed, and quality of objects manipulation [1,2]. For nearly half a century, robotic grippers have relied on various technologies, such as suction and vacuum, electrostatic and magnetic attraction, and, most widespread, mechanical gripping [3]. Since the development of gecko-inspired fibrillar polymer surfaces [4–12], a new gripping principle is now in the process of entering the market [13–19]: manipulation of objects by microfibrillar elastomer surfaces, whose adhesion can be switched on and off. Such surfaces achieve, after application of small compressive preloads, strong adhesion by van der Waals interaction and allow residue-free and silent handling, effective in both air and vacuum conditions [20–22]. These properties promise significant benefits over conventional gripping technologies, especially in manipulation of delicate and fragile objects of diverse sizes and geometries.

Object manipulation has to also work under non-ideal conditions. It has to tolerate loss of the intimate contact with the target object due to interfacial defects or due to inevitable alignment inaccuracies [23–25]. As opposed to previous assumptions, it has been proven by Tinnemann et al. [26] that the different fibrils behave largely independent from each other and can have widely distributed individual

* Corresponding author. INM – Leibniz Institute for New Materials, Campus D2 2, 66123 Saarbrücken, Germany.
E-mail address: earzt@ucsd.edu (E. Arzt).

https://doi.org/10.1016/j.jmrt.2023.09.311

adhesion strengths [26,27]. This variation comes from the different types of interfacial defects, i.e., manufacturing imperfections, surface roughness or dust and contaminations, which can lead to an unbalanced strength distribution within the fibrillar array [27]. Moreover, misalignment or unintentional off-center gripping can lead to unreliable gripping of the target object. Thus, it is crucial to monitor the correct grasping to avoid unintended loss of the object.

Microfibrillar grippers are amenable to optical observation of contact formation and breakage. In previous studies [14,26,28,29], vision based tactile sensors were used to analyze the contact of fibrillar adhesives with counter surfaces. Eason et al. [28] used frustrated total internal reflection to characterize the stress distribution on gecko toes. This technique was later adopted by Tinnemann et al. [26] to investigate in detail the detachment behavior of artificial single fibrils and fibrillar arrays. Pang et al. [14] developed and integrated a vision-based tactile sensor for a shear-induced gecko gripper to obtain real-time measurements of contact area and shear force. In our recent work [30], in-situ observation coupled with supervised learning regression models was successfully used to predict the adhesion force of microfibrillar surfaces from visual features extracted from contact images (the "contact signature"). In this first study, we demonstrated that machine learning offers several benefits for the real-time monitoring of micropatterned adhesives, surpassing the limitations of traditional numerical and analytical models.

In the present paper, we take the concept of machine learning one step further and propose an in-line monitoring system to detect the presence and correct grasping of a glass object using frustrated total internal reflection and supervised learning classification models. These models will be trained on data collected directly using a pick-and-place robotic arm. In this way, we bridge the gap from laboratory adhesion experiments to actual manipulation processes using bio-inspired microstructures with improved reliability. We argue that the implementation of machine learning in the gripping process will drastically increase the reliability, even in non-ideal gripping situations, and may hence accelerate acceptance of this novel handling technology.

2. Materials and methods

2.1. Preparation of fibrillar arrays

In the present study, eight specimens (S1–S8) of micropatterned polydimethylsiloxane (PDMS, Sylgard 184, Dow, Midland, MI, USA) with 844 mushroom shaped fibrils were fabricated using replica molding as described in earlier publications [26,29]. The fibrils had a length of $h = 1600$ μm, a stalk radius or $r = 200$ μm and a mushroom tip radius of $a \approx 300$ μm. The center-to-center distance between neighboring fibrils was $d = 800$ μm. A polished brass disc was used to seal the bottom of the mold, which replicated the smooth topography of the brass to the fibril tips. Blue pigments (PK 5091, Degussa, Essen, Germany) were added to the transparent PDMS in order to enhance the optical contrast for the in-situ imaging. Exact dimensions of the micropatterned specimens are given in Table 1.

2.2. Robot experimental steps

Experimental data was collected using a pick-and-place robotic arm (Cobot UR5, Universal Robots, Odense, Denmark), see Fig. 1 c. A transparent glass plate was used as the target object. An aluminum ring was attached on top of the object to achieve a total mass of 200, 300, and 400 g. For contact observation, the object holder was equipped with LEDs and a camera in order to implement the principle of frustrated total internal reflection as illustrated in Fig. 1 a and c. Light coupled in the transparent glass object was scattered after contacting the object with the fibrillar array, strongly improving the contrast between attached and detached fibrils [26,29]. For each specimen, 50 pick-and-place cycles were performed by picking the object from the center; in another 50 cycles the object was grasped off-center with $w \approx 3\ mm$ as can be seen in Fig. 1 b. After each cycle a random rotation of the robotic arm along the x and y axes was introduced, resulting in the misalignment angles α and β, which ranged between -2 and 2°. The glass object was cleaned with isopropanol and/or acetone after each 100 cycles to remove dust and contamination.

Before each experiment the fibrillar adhesive was mounted on the robotic arm and aligned manually with the target object. Since the robot is not equipped with a force sensor, the preload for the different specimens was chosen manually as the first full contact (position 0). The position 0 was fixed by establishing contact through visual inspection, without applying any additional load. However, a slight variation of the preload could result from handling errors. Positions 1 and 2 corresponded to lifting by 2 and 20 mm above contact, see Fig. 2 a. At the start, the robot recorded first two reference images of the contact signature, Ref-0 and Ref-2 at positions 0 and 2 for subsequent analysis. The robot arm moved at a velocity of 10 mm/s, and an acceleration of 40 mm/s^2. For detachment, the arm rotated at a rotation velocity of 25 mm/s, and an acceleration of 240 mm/s^2. In order to synchronize robot, camera, and image analysis, 1–2 s waiting time was added between the essential steps. A successful "pick" event was defined after a hold time of 10 s after moving into position 2. The robot was controlled using the UR5 control interface along with a program created using MATLAB (MathWorks, MA, USA). Fig. 2 b presents the flow chart to collect the necessary data.

2.3. Image analysis and features extraction

The images collected at position 0, 1, and 2 were analyzed using Computer Vision and Image Processing toolboxes from MATLAB as described in detail in our previous report [30]. Binary images were created by selecting a threshold gray value. Pixels with values above the threshold were defined white and were attributed to fibrils in contact, whereas pixels with smaller values were considered black, indicating non-contact regions. The mean distance between fibrils centroids, $d = 800$ μm, was used to convert from the pixel to the micrometric scale. Multiple inputs were extracted from the binarized contact signature images obtained at positions 0 and 1. The following features were extracted:

- The contact area A (A_0 at position 0 and A_1 at position 1) was obtained by calculating the number of white pixels at

Table 1 – Dimensions and quality variations of the specimens in terms of the pull-off force, F_p, the pull-off stress, σ, the stiffness of the specimen, k, the Weibull moduli, m, and the reference elongation, u_0. Data for the diameter represent mean values and standard deviations of 10 randomly selected fibrils.

Specimen	Tip radius, a (μm)	Total Number of fibrils, N	Pull-off stress, σ (N/m^2)	Pull-off force, F_p (N)	Contact stiffness, k (kN/m)	Weibull modulus, m	Reference elongation, u_0 (mm)
S1	284.39 ± 16.74	842	78.4	16.79	68.9	2.8	0.60
S2	278.86 ± 8.53	841	89.5	18.4	105.6	3.6	0.51
S3	263.97 ± 5.46	842	119.4	22.01	78.6	5.4	0.72
S4	264.30 ± 6.86	837	77.4	14.22	79.0	4.7	0.58
S5	257.30 ± 6.12	841	86.4	15.12	87.2	3.7	0.51
S6	249.56 ± 8.05	811	112.1	17.78	94.9	5.0	0.50
S7	247.72 ± 9.18	844	93.8	15.27	86.8	4.0	0.41
S8	256.27 ± 9.86	844	87.4	15.22	81.7	5.9	0.33

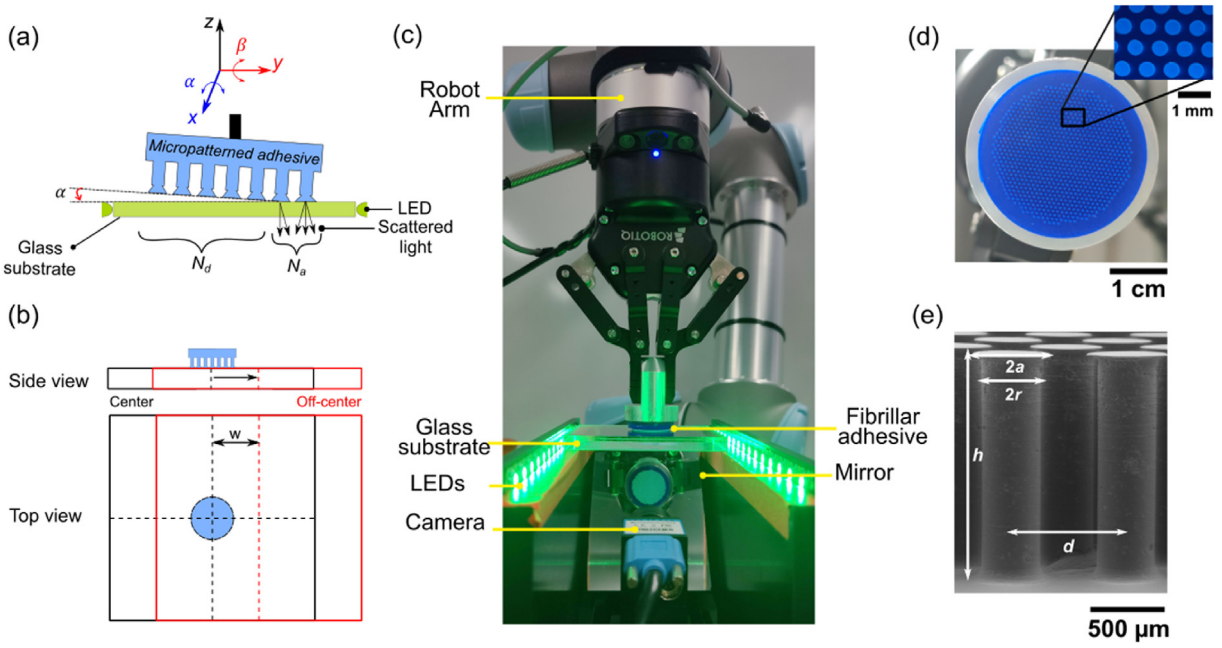

Fig. 1 – Experimental set-up for data collection. a) Schematic illustration of the micropatterned adhesive attaching to a smooth glass substrate. Frustrated total internal reflection enhances the contrast for N_a attached and N_d detached fibrils. Misorientation between the adhesive and the glass surface is introduced by robotic actuation: rotation along x and y axes, resulting in misalignment angles α and β. b) Schematic illustration of the off-center gripping where the glass object was moved in one direction with $w \approx 3$ mm. c) Robotic arm equipped with microfibrillar surface adhering to the glass. LEDs are used for the frustrated total internal reflection. A mirror reflects the contact signature to the camera. d) Image of the micropatterned specimen that typically consisted of $N = 844$ fibrils. The inset shows the hexagonal arrangement. e) Scanning electron micrograph of the mushroom-shaped fibrils.

full or partial contact, see Fig. 3 a. This feature will be sensitive to incomplete gripping due to misalignment or off-center grasping, and can potentially detect deterioration in the form of contamination or wear.

- The number of centroids in contact acquired by computer vision represented the number of attached fibrils, N_a, Fig. 3 b. Similarly, this feature will reflect missing or malformed fibrils or their deterioration over many handling cycles.
- For misaligned grasping, the position of the centroids is used to procure the misalignment vector $|\vec{v}|_0$, i.e. the vector linking the center of mass, C, of the array in full contact in Ref-0 to that in partial contact, Fig. 3c.
- The angle θ describes the misalignment vector in polar coordinates by $(|\vec{v}|, \theta)$, with $|\vec{v}|$ its magnitude and θ its angle with respect to the x axis, see Fig. 3 c.

Observations of successful or unsuccessful attachment i.e., outputs, were obtained by comparing the captured images at position 2 with Ref-2.

Since direct use of the captured images or the pixelate representation of the fibrillar contacts for a deep learning approach was limited by multiple factors (e.g. insufficient amount of data or input resolution below the receptive field size for training convolutional neural networks), the extracted

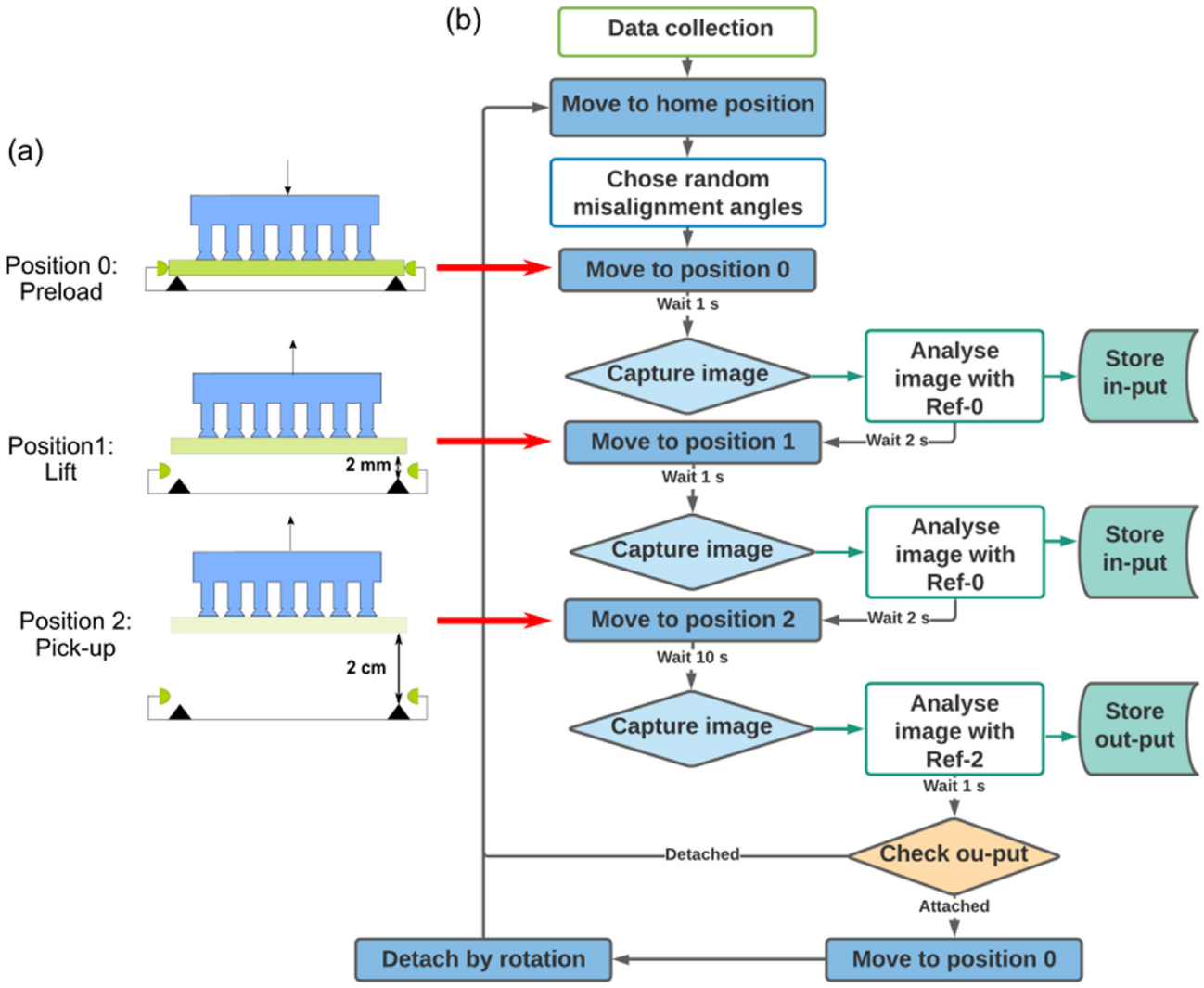

Fig. 2 – Data collection steps and flow chart. a) Schematic illustration of the three different positions for data collection. Position 0: Upon contact between array and object, a first set of visual features is extracted from the captured image (Ref-0). The robot lifts the object to position 1 and a second set of features is extracted. The object is then moved to position 2 where image capture after a hold time of 10 s decides upon a successful pick event. b) Flow chart of the experimental steps to collect data using the robot. The home position is the starting position of the robotic arm.

visual features A_0, $N_{a,0}$, $|\vec{v}|_0$, and θ_0 at position 0, and A_1, $N_{a,1}$, $|\vec{v}|_1$, and θ_1 at position 1 were used to train supervised learning models as will be presented in the next section.

2.4. *Machine learning*

For creating predictive models, we utilized supervised learning algorithms from the Statistics and Machine Learning toolbox in MATLAB (ver. R2019b). From the visual features obtained, various models were trained using MATLAB's classification learner toolbox. We focused on three models: linear Logistic Regression (LR), non-linear models Support Vector Machines (SVM), and K-Nearest Neighbors (KNN). The experimental data for the three different classifiers was divided randomly into training and testing data at a ratio of 75 to 25 (6 specimens for training and 2 for testing). In addition, a six-fold cross-validation was used to optimize the performance of the models and to avoid overfitting during training; for each iteration, 5 specimens were used for training and one for validation. A min-max normalization was used on the extracted features A_0, $N_{a,0}$, $|\vec{v}|_0$, A_1, $N_{a,1}$,and $|\vec{v}|_1$, as follows: $A' = (A - min(A))/(\max(A) - min(A))$. The features θ_0 and θ_1 were normalized by 2π such as: $\theta_i' = \theta/2\pi$.

For each of the chosen models, 3 classifiers were created. The first was trained using features extracted only from position 0 (A_0', $N_{a,0}'$, $|\vec{v}|_0'$, θ_0'), the second using the features from the image at position 1 (A_1', $N_{a,1}'$, $|\vec{v}|_1'$, θ_1'), and the final one using all the features.

The trained classifiers were evaluated by the validation accuracy calculated by $(T_p + T_n)/(T_p + T_n + F_p + F_n)$, and by plotting the confusion matrices for the test data, which included the values for true-positive, T_p (True predicted attachment), true-negative, T_n (True predicted detachment), false-positive, F_p (False predicted attachment), and false-

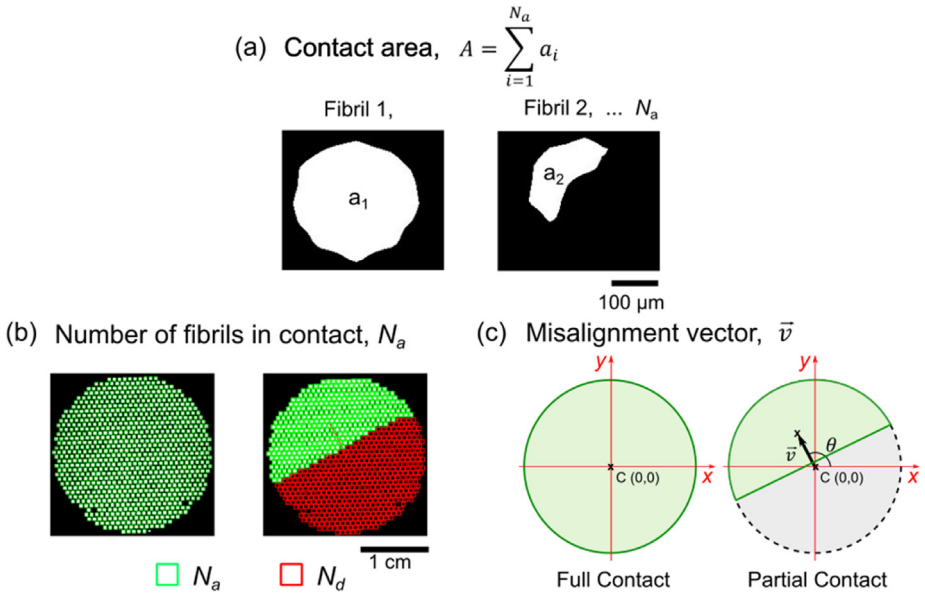

Fig. 3 – Capture of visual features corresponding to contacting fibrillar arrays. a) Full (left)/partial (right) contact of individual fibrils. The sum of the contact areas of all attached fibrils provides the total contact area, A. b) Full (left)/partial (right) contact of the array, where green corresponds to N_a attached, red to N_d non-attached fibrils. c) Misalignment vector (black arrow), $\vec{v}$, pointing from the centroid of complete contact to that of partial contact, and θ its angle with respect to the x axis.

negative, F_n (False predicted detachment). For these values, the precision, P, recall, R ,and score, F_1, can be calculated by $P = T_p/(T_p + F_p)$, $R = T_p/(T_p + F_n)$ and $F_1 = 2PR/(P+R)$.

2.5. *Adhesion properties of the specimens*

To characterize the quality of the 8 specimens, pull-off forces and statistical properties of the fibrillar adhesives were measured using a customized tensile tester (Inspekt table BLUE, Hegewald & Peschke, Nossen, Germany) equipped with a 50 N load cell, a camera, and the frustrated-TIR system for in-situ observation. The array was brought into contact with the target object (a smooth glass substrate), at a velocity of 1 mm/min until a prescribed compressive load of 1 N, was reached. The array was then instantly retracted at the same velocity. The highest tensile force was reported as the pull-off force, F_p. The stiffness, k, of the fibrillar surface was obtained from force-displacement curves in the compressive regime after deducing the load cell stiffness: $k_{50} = 134.6$ Nmm^{-1} (from $1/k = 1/k_{slope} - 1/k_{50}$). Videos of the tests were recorded and correlated with the force-displacement measurement. To characterize the spread of the distribution of individual fibril pull-off forces, a cumulative Weibull distribution was fitted (Equation 1 in the supporting information, see also [31,32]. The Weibull moduli, m, and the reference elongations, u_0, of the arrays are reported in Table 1.

3. Results and discussion

3.1. *Distributions of fibril and of array strengths*

The pull-off force measured for the different specimens ranged between 14 N for the weakest array S4 and 22 N for the strongest array S3, see Table 1. As the glass surface was free of contaminants, the likely reason for this distribution lies in the limitations of the replica molding process: surface defects and deviations in fibril radius induced a spread in pull-off strength across each array. These variations were quantified by fitting Weibull distributions (equation 1 in SI) and extracting characteristic values as explained in previous reports [27,31,32], and presented in Table 1.

3.2. *Contact signatures for misaligned gripping*

Fig. 4 a, b, and c show the random distribution of the misalignment angles α and β chosen during data collection for different object masses. Fig. 4 d displays contact signatures at preload for specimens S1 (i and ii) and specimens S2 (iii) divulging the variation of the number of attached fibrils N_a for similar misalignment angles ($\alpha \sim 0.6°$ and $\beta \sim 0.02°$). This variation is a result of the slight preload variation from the manual definition of position 0 for the different specimens. Moreover, the robot arm has a repeatability error of 100 µm when reaching a preset position. This can explain the significant difference in number of attached fibrils, N_a, for a similar preset values of α and β between different specimens ($N_{a,S1} = 566$ and $N_{a,S2} = 482$) and for two cycles of the same specimen ($N_{a,S1\ (i)} = 566$ and $N_{a,S1\ (ii)} = 601$).

The patterned adhesives were successfully used to train the pick-and-place handling of glass objects with a mass of 200, 300, and 400 g. The data set obtained comprised 800 data points for each of the objects. This data included intentional variations such as the preset degrees of misalignment or balanced/unbalanced gripping due to variations of the gripping position, and unpremeditated variations attributed to specimens' quality variations, inaccuracies in robot arm movements or slight preload variations.

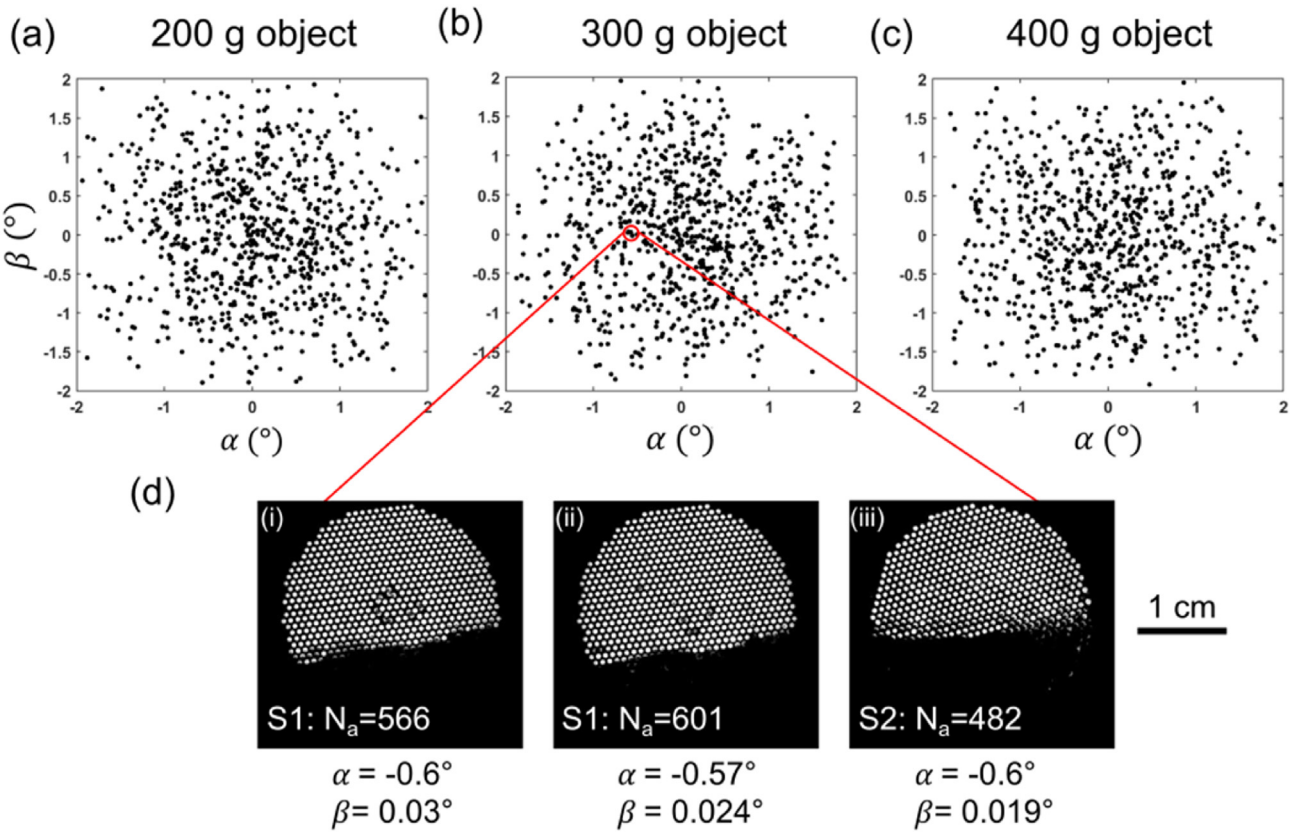

Fig. 4 – Intentional variation of the misalignment. a-c) Rotation angles of the robotic arm β versus α, both ranging between −2 and 2°. Misorientation data for the different objects with mass a) 200 g, b) 300 g, and c) 400 g. d) Exemplary images of the contact at preload for specimens S1 (i and ii) and S2 (iii) with similar rotation angles, showing a variation in the number of fibrils in contact, N_a.

3.3. *Effect of misalignment and off-center gripping*

Fig. 5 shows the combined effect of misaligned contact and off-center gripping after lifting the object to position 1. The unbalanced attachment induces a moment, M, leading to a rotation of the glass object. In Fig. 5 a, the rotation of the glass is similar to the rotation of the robotic arm (anti-clockwise) around the x axes, which leads to attachment of additional fibrils and counters the detachment, as can be seen on the image (a.1) at position 1. In contrast when the rotation of the object is in the opposite direction to the robot arm rotation, a peeling moment is created and fast detachment can be observed, see Fig. 5 b, image (b.1). The aim of the machine learning process is to anticipate these processes and thereby increase the reliability of handling.

Fig. 6 depicts the misalignment vector $\vec{v}$ ($|\vec{v}|$,θ) in the polar coordinate system, grouped by the output results for the different object masses. The distance of each dot to the center corresponds to the length of the vector, $|\vec{v}|$, ranging between 0 and 10 mm. The angle of the misalignment vector, θ, is designated by the position of the dots in the polar plot and ranges between 0 and 2π. The blue dots represent successful attachment, while the red dots correspond to detachment (unsuccessful attachment). Fig. 6 a, c, and e correspond to data collected at position 0, i.e., at maximum preload. The fraction of successful attachments decreased with increasing object mass: for the lighter (200 g) object, 71.4 % of the manipulations were successfully attached while only 38.1 % of the trials were successful with the 400 g object. For the 300 g object, the attachment to detachment ratio was about 1:1, see Table S1 in SI. Fig. 6 b, d, and f correspond to data collected at position 1.

The misalignment vector data collected at position 0 appears to be condensed around the center. After lifting the object to position 1 some of the data signifying detachment (red dots) expand in the y direction as the misalignment vector elongates. This can be related to the off-center gripping shown in Fig. 5 b, where the peeling moment leads to the detachment of some fibrils after lifting and causes detachment of the object. The blue dots (attachments) on the other hand congregate around the center because in some cases the off-center gripping improves the contact during lifting as can be seen in Fig. 5 a. The effect of off-center gripping on the misalignment vector after lifting increases as the mass of the glass object increases (the expansion and congregation of the data for the 400 g object is more pronounced than for the 200 g).

3.4. *Supervised machine learning*

The normalized features, collected from the contact images at position 0 (A'_0, $N'_{a,0}$, $|\vec{v}|'_0$, θ'_0), and position 1 (A'_1, $N'_{a,1}$, $|\vec{v}|'_1$, θ'_1), were implemented into supervised machine learning models

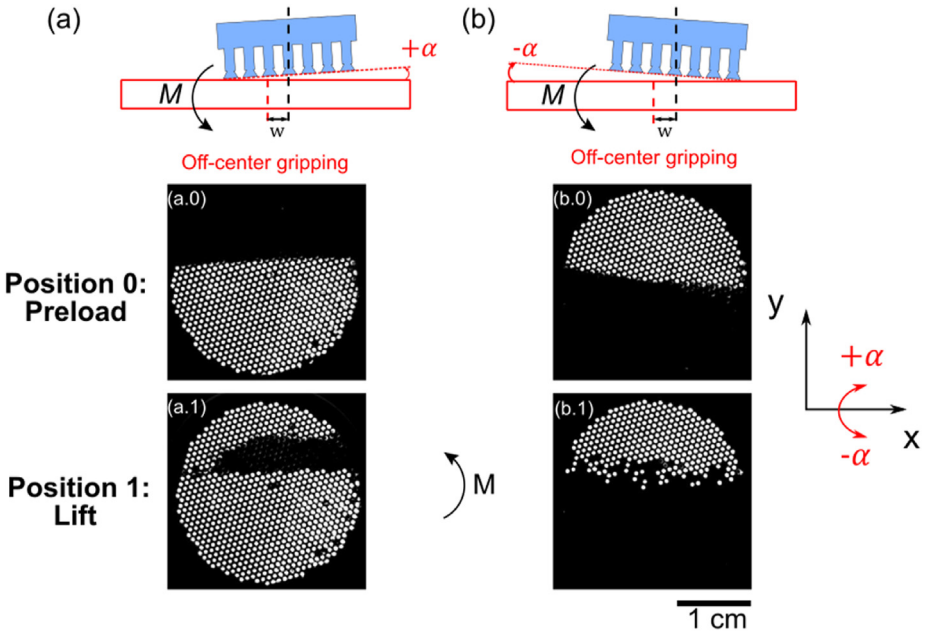

Fig. 5 – Rotation of the object during off-center attachment. a) The object rotates anti-clockwise similar to the rotation of the robotic arm; this reduces the initial misalignment and leads to attachment of previously detached fibrils (upper moon-shaped area in a.1). b) The object rotates oppositely to the rotation of the robotic arm, which increases misalignment, reduces the contact area, and leads to peeling.

to train and compare multiple classifiers. The classification models enable the prediction of attachment/detachment depending on the mass of the object. Fig. 7 a depicts the accuracy of the training data as a function of the object mass for three different classifiers: support vector machines (SVM), logistic regression (LR), and the k-nearest neighbor (KNN). For all trained classifiers the accuracies obtained were always higher than 90%, with KNN exhibiting an 100 % validation accuracy and LR showing the lowest accuracy (~90%). However, this trend changes when testing the models with the remaining testing data. Fig. 7 b shows the score of the testing data for the different trained classifiers. LR scores highest for the 200 g object at 95 % and for the 300 g object at 90 %. SVM has the highest score for the 400 g and comes in second for the other classifiers. The testing of KNN reveals the incapability of the model to adapt to new data as the score of the KNN comes in the third position for the three different object masses.

The confusion matrices in Fig. 8 and the column graphics in Fig. 9 depict the comparison of LR trained first with features extracted at position 0, P_0 (A'_0, $N'_{a,0}$, $|\vec{v}|'_0$, θ'_0) (Fig. 8 a), at position 1, P_1 (A'_1, $N'_{a,1}$, $|\vec{v}|'_1$, θ'_1) (Fig. 8 b), and the combined features from position 0 and 1, $P_{0,1}$ (Fig. 8 c). The number of false positives, F_p, and false negative, F_n, diminished when features obtained at lifting position were included in the training. For the 200 g object for example, 21 data points out of 40 true detachments were falsely predicted as attached when using only features from position 0, 16 when using features from position 1, and only 4 when using all features. The effect of the unbalance distribution of the two result groups in the collected data is shown in the confusion matrices for the 200 and 400 g objects by the large variation between the true positives and true negatives.

As can be seen in Fig. 9, the classifier P_0 has the lowest score with a maximum of ~90 % for the 200 g object and only 71 % for the 400 g object. This drop can be explained by the lack of information in the data at position 0 about the off-center gripping, where the influence is more pronounced for the heavier objects. The score for the 400 g increases to 84 % for the classifier P_1, as more information is included. Combining the features in both positions (position 0 and 1) resulted in an increase of the accuracy and score for all the classifiers $P_{0,1}$ to more than 90 %. The remaining 5–9% for perfect prediction could be attributed to the unbalanced distribution of the two result groups (attached/detached) in the collected data, see Table S1 in SI, and to the undesirable variations that are not fully shown in the obtained features, which may induce wrong classification. The confusion matrices and classifiers comparisons of the SVM, and KNN models are shown in Figs. S2 and S3 in the SI. The accuracy, precision, recall, and score of all the models are presented in Tables S2–S10 in SI.

Overall, the high prediction accuracies demonstrated in this paper as a result of in-situ observation at two positions are encouraging as the method can therefore significantly increase the reliability of object handling with micropatterned adhesives. In particular, inclusion of data from the lift position to train the classification models will allow an impending peeling to be readily anticipated; dramatic detachments and loss of object could hence be avoided. Also, the reliability of handling asymmetric objects with various geometries and forms can profit. More specifically, the data collected directly using the robotic arm bridge the gap between laboratory adhesion experiments in displacement-control and the actual pick and place application under force-controlled loading [31,33].

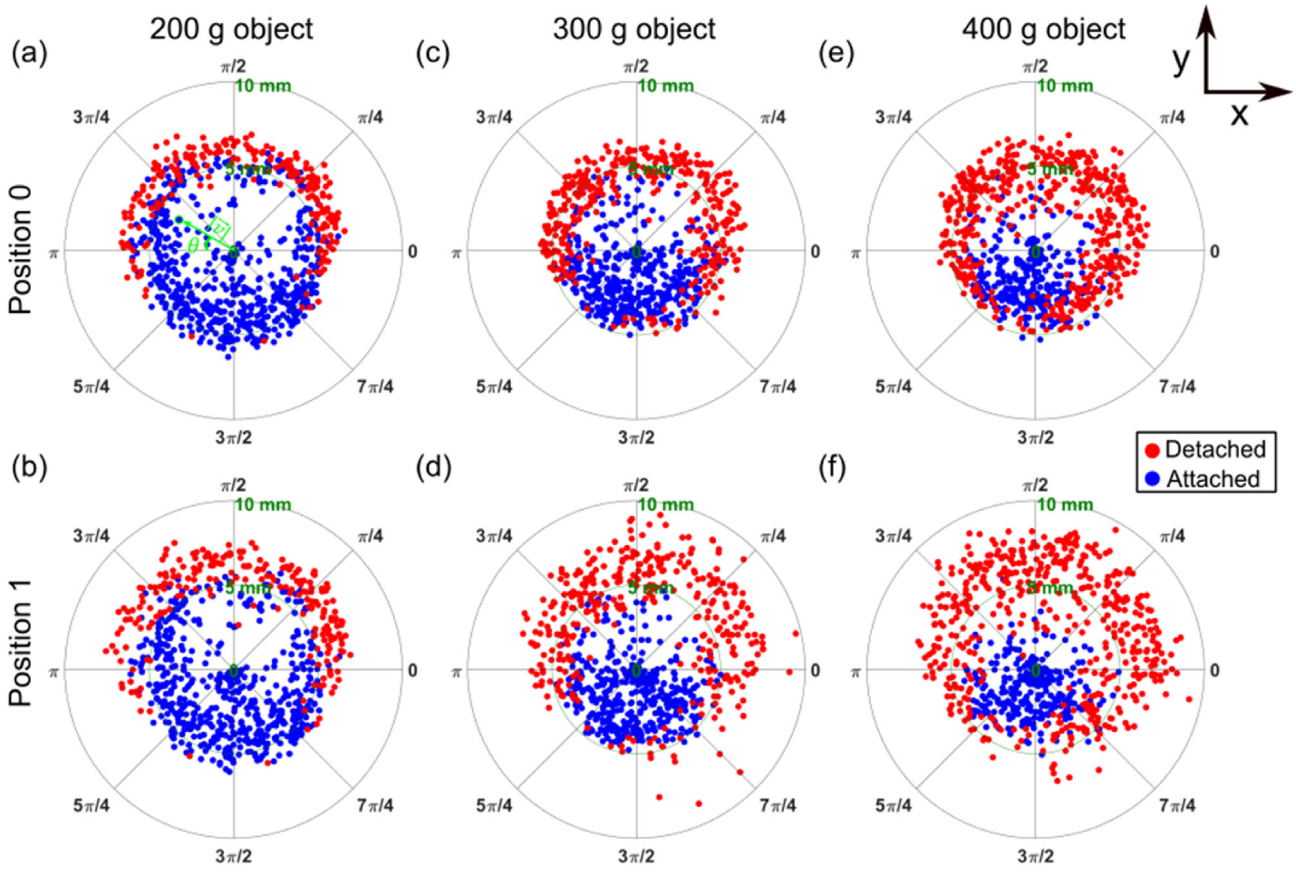

Fig. 6 – Misalignment vector, $\vec{v}$ in polar coordinate grouped by the output results successful (blue) and unsuccessful attachment (red). Upper row (a,c,e) corresponds to contact images collected at preload (position 0), whereas the lower row (b,d,f) corresponds to contact images collected upon lifting at position 1. Columns correspond to the masses of the object of 200, 300, and 400 g. Each dot represents the length of the vector, $|\vec{v}|$ ranging between 0 and 10 mm and the misalignment angle, θ. The asymmetric character of these plots results from the off-center gripping coming from one direction.

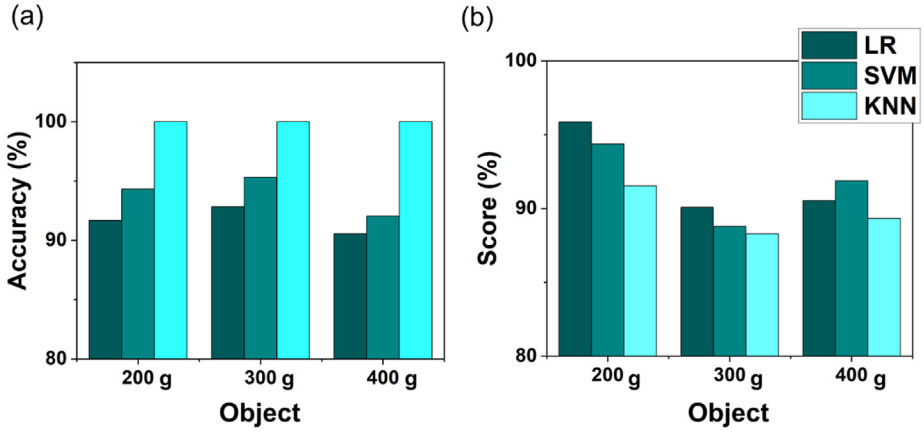

Fig. 7 – Classification results of three classifiers. a) The validation accuracy (training) and b) the score (testing) of the support vector machines (SVM), logistic regression (LR), and k-nearest neighbors (KNN) trained by the three objects.

Certain limitations of the present approach should be noted. The trained models are highly related to the relevant application circumstances, such as object weight, trajectory of the robot arm, and waiting times between different steps. Moreover, possible effects of additional parameters such as velocity and acceleration of the robot arm were not taken into consideration. Based on our feasibility study, more extensive coverage of the complex parameter space under

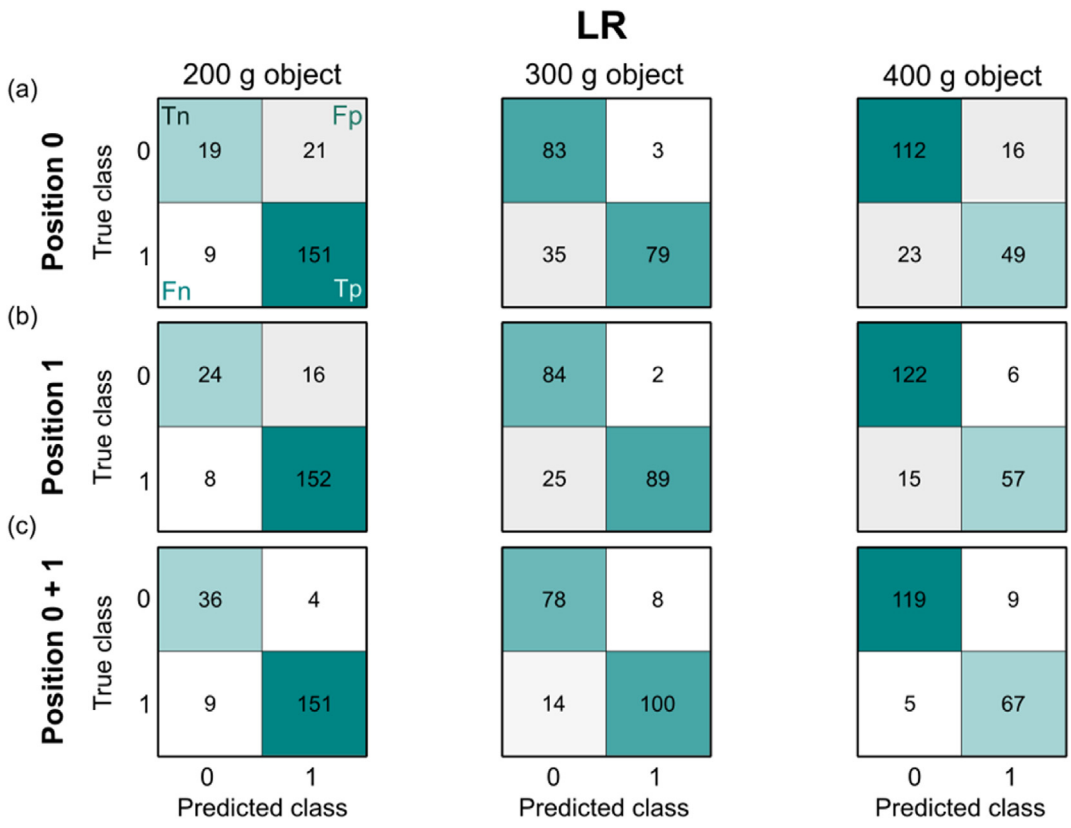

Fig. 8 – Confusion matrices of the different classifiers trained with the logistic regression (LR) model with 1 is the case of successful attachment and 0 is detachment. Each matrix represents the total number of true negative (T_n), true positive (T_p), false negative (F_n) and false positive (F_p). Columns correspond to the masses of the object of 200, 300, and 400 g. a) Classifiers P_0 trained using data at preload (position 0). b) Classifiers P_1 trained using data upon lifting (position 1). c) Classifiers $P_{0,1}$ trained using data from positions 0 and 1.

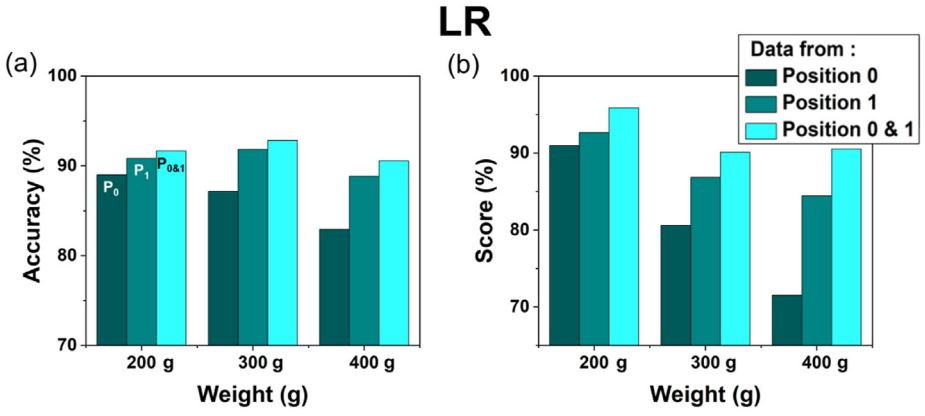

Fig. 9 – Comparing input data for the logistic regression (LR) model. a) The validation accuracy (training) and b) the score (testing) of three objects with the mass 200, 300, and 400 g when trained by data from position 0 (P_0), position 1 (P_1), and position 0 and 1 ($P_{0,1}$).

realistic handling conditions can be performed to validate the technique suggested here. Such optimization of the experimental training data as well as development of new optical techniques compatible with opaque and rough objects will bear great potential to significantly improve in-line control of handling processes even in demanding conditions.

4. Conclusions

In this work, we present an in-line monitoring system using supervised learning classification models, optical observation, and image processing. Three classification models were trained and tested using visual features obtained from the

contact signature at preload and after lifting the glass object. Successful and unsuccessful attachment of the object was demonstrated in a pick and place application. The following conclusions can be drawn:

- The performance of a micropatterned adhesives can be affected by intentional or unintentional variations, notably, prescribed misalignment and off-center gripping or quality of the adhesive and preload/displacement variations attributed to the limited robot arm accuracy.
- All tested classifiers showed accuracies higher than ~ 90% for predicting impending attachment or detachment as a function of the objects mass. The highest testing score was obtained for logistic regression.
- Observation of the contact signature at compressive preload alone, i.e. before lifting of the object, resulted in a high predictive capability (between 70 and 90 %). Including data from the lifting position significantly increased the accuracy and score of the different trained models (to more than 90 %).

The present machine learning approach is proposed as a means of enhancing the reliability of handling with micropatterned adhesives. Further exploration of the complex parameter space in handling realistic objects is warranted to validate the technique proposed here. It is also suggested that the technique can be used to identify degradation and wear of the polymeric micropatterns, both of which can impair the reliability of the handling process.

Credit author statement

Samri Manar: Conceptualization, Methodology, Investigation, Software, Writing- Original Draft. Jonathan Thiemecke: Software. René Hensel: Supervision, Conceptualization, Writing - Review & Editing. Eduard Arzt: Supervision, Conceptualization, Writing - Review & Editing, Funding acquisition.

Data availability

The data that support the findings of this study are available from the corresponding authors upon reasonable request.

Declaration of competing interest

The authors declare the following financial interests/personal relationships which may be considered as potential competing interests: Eduard Arzt declares that he is co-owner of a start-up commercializing micropatterned adhesives.

Acknowledgements

We acknowledge funding by the Leibniz Competition Grant MUSIGAND (No. K279/2019). Lisa Sold, INM, assisted with data collection during pick and place experiments.

Appendix A. Supplementary data

Supplementary data to this article can be found online at https://doi.org/10.1016/j.jmrt.2023.09.311.

REFERENCES

[1] Lindström V, Winroth M, Stahre J. Ergonomia 2008;30.
[2] Katz RL, Koutroumpis P. SSRN. Electron J 2012 (May 29, 2012). Available at SSRN: https://ssrn.com/abstract=2070035.
[3] Fantoni G, Santochi M, Dini G, Tracht K, Scholz-Reiter B, Fleischer J, et al. CIRP Ann - Manuf Technol 2014;63:679–701.
[4] Parness A, Soto D, Esparza N, Gravish N, Wilkinson M, Autumn K, et al. J R Soc Interface 2009;6:1223–32.
[5] Lee H, Lee BP, Messersmith PB. Nature 2007;448:338–41.
[6] Davies J, Haq S, Hawke T, Sargent JP. Int J Adhesion Adhes 2009;29:380–90.
[7] Murphy MP, Kim S, Sitti M. ACS Appl Mater Interfaces 2009;1:849–55.
[8] King DR, Bartlett MD, Gilman CA, Irschick DJ, Crosby AJ. Advanced materials. 2014.
[9] Heepe L, Gorb SN. Annu Rev Mater Res 2014;44:173–203.
[10] Autumn K, Liang YA, Hsieh ST, Zesch W, Chan WP, Kenny TW, et al. Nature 2000;405:681–5.
[11] Autumn K, Puthoff J. Biological adhesives. Cham: Springer International Publishing; 2016. p. 245–80.
[12] Autumn K, Gravish N. Phil Trans Math Phys Eng Sci 2008;366:1575–90.
[13] Glick P, Suresh SA, Ruffatto D, Cutkosky M, Tolley MT, Parness A. IEEE Rob Autom Lett 2018;3:903–10.
[14] Pang C, Mak K, Zhang Y, Yang Y, Tse YA, Wang MY. In: 2021 IEEE international conference on robotics and automation (ICRA). IEEE; 2021. p. 736–42.
[15] Hawkes EW, Christensen DL, Han AK, Jiang H, Cutkosky MR. Proceedings - IEEE international conference on robotics and automation. Institute of Electrical and Electronics Engineers Inc.; 2015. p. 2305–12.
[16] Hawkes EW, Jiang H, Cutkosky MR. Int J Robot Res 2016;35:943–58.
[17] Dadkhah M, Zhao Z, Wettels N, Spenko M. IEEE international conference on intelligent robots and systems. Institute of Electrical and Electronics Engineers Inc.; 2016. p. 1006–11.
[18] Jiang H, Hawkes EW, Fuller C, Estrada MA, Suresh SA, Abcouwer N, et al. A robotic device using gecko-inspired adhesives can grasp and manipulate large objects in microgravity. 2017.
[19] Song S, Majidi C, Sitti M. IEEE international conference on intelligent robots and systems. Institute of Electrical and Electronics Engineers Inc.; 2014. p. 4624–9.
[20] Autumn K, Sitti M, Liang YA, Peattie AM, Hansen WR, Sponberg S, et al. Proc Natl Acad Sci USA 2002;99:12252–6.
[21] Purtov J, Frensemeier M, Kroner E. ACS Appl Mater Interfaces 2015;7:24127–35.
[22] Sameoto D, Sharif H, Menon C. J Adhes Sci Technol 2012;26:2641–52.
[23] Barreau V, Hensel R, Guimard NK, Ghatak A, McMeeking RM, Arzt E. Adv Funct Mater 2016;26:4687–94.
[24] Booth JA, Bacca M, McMeeking RM, Foster KL. Adv Mater Interfac 2018;5.
[25] Bacca M, Booth JA, Turner KL, McMeeking RM. J Mech Phys Solid 2016:428–44.
[26] Tinnemann V, Hernández L, Fischer SCL, Arzt E, Bennewitz R, Hensel R. Adv Funct Mater 2019;29:1807713.

[27] Booth JA, Hensel R. Appl Phys Lett 2021;119:230502.
[28] v Eason E, Hawkes EW, Windheim M, Christensen DL, Libby T, Cutkosky MR. Bioinspiration Biomimetics 2015;10:016013.
[29] Thiemecke J, Hensel R. Adv Funct Mater 2020;30.
[30] Samri M, Thiemecke J, Prinz E, Dahmen T, Hensel R, Arzt E. Materials today. 2022.
[31] Hensel R, Thiemecke J, Booth JA. ACS Appl Mater Interfaces 2021;13:19422–9.
[32] Booth JA, Tinnemann V, Hensel R, Arzt E, McMeeking RM, Foster KL. J R Soc Interface 2019;16.
[33] Suresh SA, Hajj-Ahmad A, Hawkes EW, Cutkosky MR. J R Soc Interface 2021;18.